Journal of Materials Chemistry A

ROYAL SOCIETY OF CHEMISTRY

PAPER

View Article Online
View Journal | View Issue

Cite this: J. Mater. Chem. A, 2022, 10, 12464

A dopant-free 2,7-dioctyl[1]benzothieno[3,2-*b*][1]benzothiophene (C8-BTBT)-based hole transporting layer for highly stable perovskite solar cells with efficiency over 22%†

İsmail Cihan Kaya, [ab] Resul Ozdemir, [c] Hakan Usta [c] and Savas Sonmezoglu *[ad]

Received 25th February 2022
Accepted 13th May 2022

DOI: 10.1039/d2ta01541b

rsc.li/materials-a

In this study, for the first time, n–i–p PSCs were fabricated using dopant-free 2,7-dioctyl[1]benzothieno[3,2-*b*][1]benzothiophene (C8-BTBT) as the solution-processed hole transporting layer (HTL). The power conversion efficiency (PCE) of the optimized device with the C8-BTBT film that favored edge-on molecular alignment was 22.45% with negligible hysteresis. A thinner dopant-free C8-BTBT HTL effectively protected the perovskite layer from moisture resulting in better shelf-life stability for un-encapsulated PSCs, which maintained >80% of its initial PCE (after a period of 120 days) at a relative humidity level of 40–45%. In addition, the C8-BTBT-based PSCs kept their high performance with no obvious PCE loss at 60 °C for 20 days in the ambient atmosphere and retained 82% of their initial PCE at 85 °C for 10 days. Overall, our findings revealed that a thin solution-processed C8-BTBT HTL plays a critical role not only in hole extraction and transport but also in greatly improving the ambient and thermal stability of n–i–p PSCs.

Introduction

Organic–inorganic hybrid perovskite solar cells (PSCs) have emerged as one of the most promising photovoltaic technologies in the past decade owing to their very high-power conversion efficiencies (PCEs) and facile low-cost fabrication.[1–4] However, long-term ambient instability and thermal instability still remains the most critical issues to be resolved for successful commercialization of this technology.[5,6] Since a typical high performance PSC device has a relatively simple device structure consisting of a perovskite active layer sandwiched between charge transporting layers (*i.e.*, the electron transporting layer (ETL) and hole transporting layer (HTL)), device instability is generally associated with a degradation in these layers under various internal/external factors such as humidity, temperature, oxygen, UV illumination, and ion diffusion.[7–12] Recent studies have demonstrated that organic HTL materials could play a considerable role in the stability of n–i–p PSCs by forming a top protective layer (*i.e.*, physical barrier against various ambient species) on the perovskite active film.[13,14] Although HTLs employed in PSCs could also be an organometallic compound or a conducting polymer, small molecules have attracted a lot of attention due to their well-defined structures, facile synthesis/purification, high chemical purity, and reproducible film forming ability.[15–20] In most of the high-efficiency PSCs, 2,2′,7,7′-tetrakis(*N*,*N*-di-*p*-methoxyphenylamine)-9,9′-spirobifluorene (spiro-OMeTAD) small molecules have been used as an HTL material owing to its outstanding physicochemical/optoelectronic properties.[21–24] However, a spiro-OMeTAD layer suffers from low intrinsic hole mobility, and hygroscopic p-type dopants (*e.g.*, Li-TFSI and TBP) are typically required to enhance its electrical properties[15,25] for high photovoltaic performance. The hygroscopic nature of the dopants generally leads to faster device degradation, and these dopants have a tendency to migrate into the perovskite active layer.[26–29] On the other hand, high synthesis and film fabrication costs for spiro-OMeTAD are additional key issues awaiting a solution.[30] Therefore, considerable recent research efforts have been focused on alternative dopant-free solution-processable HTL molecules with the ultimate goal of achieving long-term ambient and thermal stability with high photovoltaic performance.[31–33] An effective dopant-free HTL molecule would require a combination of several key properties such as solubility in organic solvents that are orthogonal to

[a]Nanotechnology R&D Laboratory, Karamanoğlu Mehmetbey University, Karaman, Turkey. E-mail: svssonmezoglu@kmu.edu.tr

[b]Department of Metallurgical & Materials Engineering, Konya Technical University, Konya, Turkey

[c]Department of Nanotechnology Engineering, Abdullah Gül University, 38080 Kayseri, Turkey

[d]Department of Metallurgical & Materials Engineering, Karamanoğlu Mehmetbey University, Karaman, Turkey

† Electronic supplementary information (ESI) available. See https://doi.org/10.1039/d2ta01541b

perovskite, proper frontier orbital energies/topographies, and good film forming and hole transport abilities in the undoped state. To this end, a number of dopant-free HTL molecules with varied π-architectures (*e.g.*, star-shaped, fused, and donor–acceptor) and structures have recently been developed to improve the long-term stability of PSC devices.[34–36] The majority of these molecules are inspired by the spiro-OMeTAD π-structure and include arylamino moieties. Therefore, a fundamental question arises as to whether a π-framework without arylamino units could ever enable PSCs with good device performance and long-term ambient stability. Considering that there are a large number of solution-processable semiconducting π-structures developed in the last three decades with varied physicochemical/optoelectronic properties for different fields of optoelectronics and most of these semiconductors are yet to be explored in PSCs, we envision that a rationally decided high mobility p-type molecular semiconductor with a wide optical band gap and relatively simple synthesis/purification could be a perfect HTL candidate.

Among all the solution-processable p-type molecular semiconductors realized to date, dialkyl-substituted [1]benzothieno[3,2-*b*][1]benzothiophene (BTBT) derivatives, especially 2,7-dioctyl[1]benzothieno[3,2-*b*][1]benzothiophene (C8-BTBT) (Fig. 1), stand out as a champion semiconductor family with great film forming ability, very high hole mobilities (μ_h = 30–40 $cm^2\ V^{-1}\ s^{-1}$), stabilized HOMO energy levels (−5.5 eV), and good ambient stability.[37–40] A C8-BTBT film forms very favorable metal–semiconductor interfaces with a Au electrode for efficient charge injection/extraction. The HOMO level of C8-BTBT matches well with the valence band of perovskites (VB = −5.5 eV for $(CsI)_{0.05}(FAPbI_3)_{0.85}(MAPbBr_3)_{0.15}$) for efficient hole extraction. BTBT-based small molecules have found widespread application in various optoelectronic devices including organic field-effect transistors,[41,42] photodetectors[43] and solar cells.[44] C8-BTBT has a fused rigid π-system with structural symmetry and high coplanarity enabling large frontier orbital coefficients on the sulfur atoms to form a favorable electronic structure in the solid-state for efficient hole transport. The phene-like π-electronic structure of the BTBT core results in wide optical band gaps (3.5 eV) and high LUMO energy levels (−2.0 eV) that could effectively block undesired electron flow from the perovskite active layer (CB = −3.8 eV for $(CsI)_{0.05}(FAPbI_3)_{0.85}(MAPbBr_3)_{0.15}$).[37] The good hydrophobicity of the spin-coated C8-BTBT film originates from its densely packed microstructure with alkyl substituents pointing towards the air-film interface, and it could be very beneficial to improve the ambient stability of the perovskite active layer, especially when it is used in n–i–p device architecture. Using this hydrophobicity, some of us have previously demonstrated that micro-/nano-structured C8-BTBT films could enable the formation of nanoscopic thin metallic films for highly efficient surface-enhanced Raman spectroscopy (SERS).[45] From a material production point of view, unlike the majority of high mobility semiconductors, the synthesis of C8-BTBT is a relatively straightforward three-step transition-metal-free process involving the commonly used Friedel–Crafts acylation/Wolff–Kishner reduction reactions (Scheme S1, ESI†). Also, without any tedious purification for the intermediate compounds, single chromatographic purification in the final step is sufficient to reach an electronic grade purity level for C8-BTBT. We are capable of synthesizing highly pure C8-BTBT on the multigram scale in our laboratory. Despite all promises, to the best of our knowledge, C8-BTBT has never been studied in n–i–p PSCs as an HTL. A detailed literature search revealed that C8-BTBT has been used with $CH_3NH_3PbI_3$ perovskite in heterojunction and bilayer architectures to fabricate photodetectors,[46–48] which showed efficient extraction/transport of photogenerated holes in the perovskite conduction band due to favorable C8-BTBT/perovskite and Au/C8-BTBT/perovskite interfaces. In another study, C8-BTBT has been exploited to replace PEDOT:PSS in p–i–n PSCs to improve the ambient stability of PSCs.[44] However, in this device architecture, the C8-BTBT layer was designed to be under the perovskite active layer and, therefore, the contribution of its hydrophobic nature to device stability remained limited (~20% drop in PCE in only seven days). Also, very recently C8-BTBT has been used as an interfacial defect passivation layer between the perovskite and the spiro-OMeTAD layers in n–i–p PSCs.[49] It was revealed that C8-BTBT reduced nonradiative recombination at the surface and improved charge carrier collection and transport, which in the end led to improved PCEs. In this study, however, the

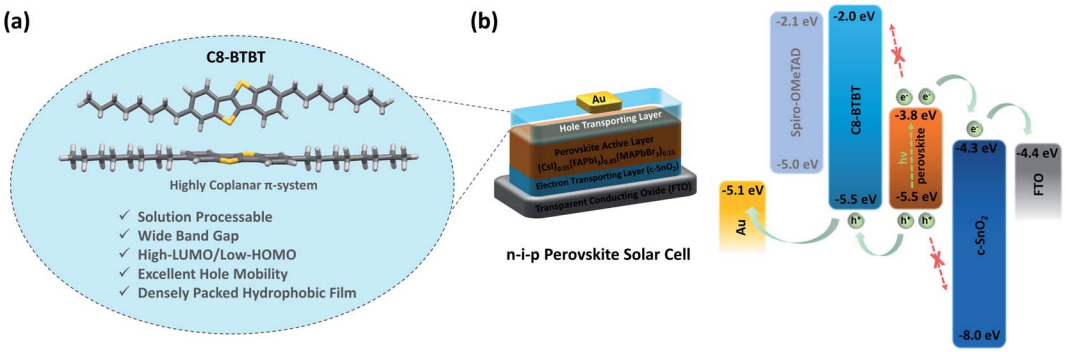

Fig. 1 (a) The chemical structure of C8-BTBT and its favorable physicochemical/electronic properties for use as the HTL in perovskite solar cells. (b) The device structure and the energy level diagram of the n–i–p perovskite solar cell (FTO/c-SnO_2/$(CsI)_{0.05}(FAPbI_3)_{0.85}(MAPbBr_3)_{0.15}$/C8-BTBT/Au) fabricated in this study showing the schematic of exciton formation/dissociation and charge transport. The frontier orbital energy levels of spiro-OMeTAD are provided for comparison.

utilization of spiro-OMeTAD as the HTL was still limiting the thermal stability of the devices.

Herein, we develop a highly efficient and stable n–i–p structured perovskite solar cell by designing a dopant-free HTL based on C8-BTBT, which synergistically integrates several key properties for use in perovskites. Along with its outstanding power conversion efficiency of 22.45%, dopant-free C8-BTBT HTL-based perovskite solar cells exhibited an excellent long-term stability (>80% of $PCE_{initial}$ after 120 days) at 40–45% relative humidity (RH) without encapsulation at room temperature. This is remarkable especially when compared with the control devices fabricated with the same device architecture with a benchmark doped spiro-OMeTAD HTL (~19% of $PCE_{initial}$ after 120 days). Moreover, C8-BTBT also improved the thermal stability of the solar cells, which maintained their initial PCE after aging at 60 °C for 20 days. In addition, the devices fabricated with C8-BTBT retained 82% of their initial PCE at 85 °C for 10 days, whereas the PCE of the control device fabricated with a doped spiro-OMeTAD HTL decreased sharply at 85 °C.

Results and discussion

The synthesis of C8-BTBT was carried out in three steps in accordance with a reported procedure (Scheme S1, ESI†).[37,50] A white crystalline C8-BTBT solid with high chemical purity was obtained in 77% yield (final step) by flash column chromatography using silica gel/hexane as the stationary/mobile phases. The molecular structure and purity of C8-BTBT were verified by $^{1}H/^{13}C$ NMR spectroscopies, mass spectrometry, and elemental analysis (Fig. S1–S3, ESI†).

In order to investigate the hole transporting layer characteristics of C8-BTBT, n–i–p PSCs were fabricated with the device architecture of fluorine-doped tin-oxide (FTO)/c-SnO_2/$(CsI)_{0.05}(FAPbI_3)_{0.85}(MAPbBr_3)_{0.15}$/HTL/Au (Fig. 1(b)). A dopant-free C8-BTBT layer was spin-coated onto the perovskite film from chlorobenzene solution, and also comparative PSC devices were fabricated with a doped spiro-OMeTAD HTL. The cross-sectional SEM images of the completed devices using doped spiro-OMeTAD and dopant-free C8-BTBT are shown in Fig. 2(a) and (b), respectively. The thicknesses of all layers except the HTLs are the same in both PSC devices. The thickness of the spiro-OMeTAD layer is ~200 nm whereas that of C8-BTBT is only ~50 nm. Despite having a much lower thickness, C8-BTBT uniformly covers the perovskite surface, which could effectively suppress parasitic recombination and minimize current leakage. The surface morphologies for spiro-OMeTAD and C8-BTBT films deposited on the perovskite layer are shown in Fig. 2(c) and (d), respectively, which indicate very homogeneous and uniform coating on the perovskite surface. On the other hand, despite the pinhole-free morphology in both HTLs, some white particles are observed on the surface of spiro-OMeTAD (shown by red circles in Fig. 2(c)) that can be ascribed to the aggregation of the Li-TFSI additive.[51]

The microstructural and morphological characterization studies of the current HTLs on the (FTO)/c-SnO_2/$(CsI)_{0.05}(FAPbI_3)_{0.85}(MAPbBr_3)_{0.15}$ substrates were performed by using θ–2θ out-of-plane X-ray diffraction (XRD) scans (Fig. 3(a)) and

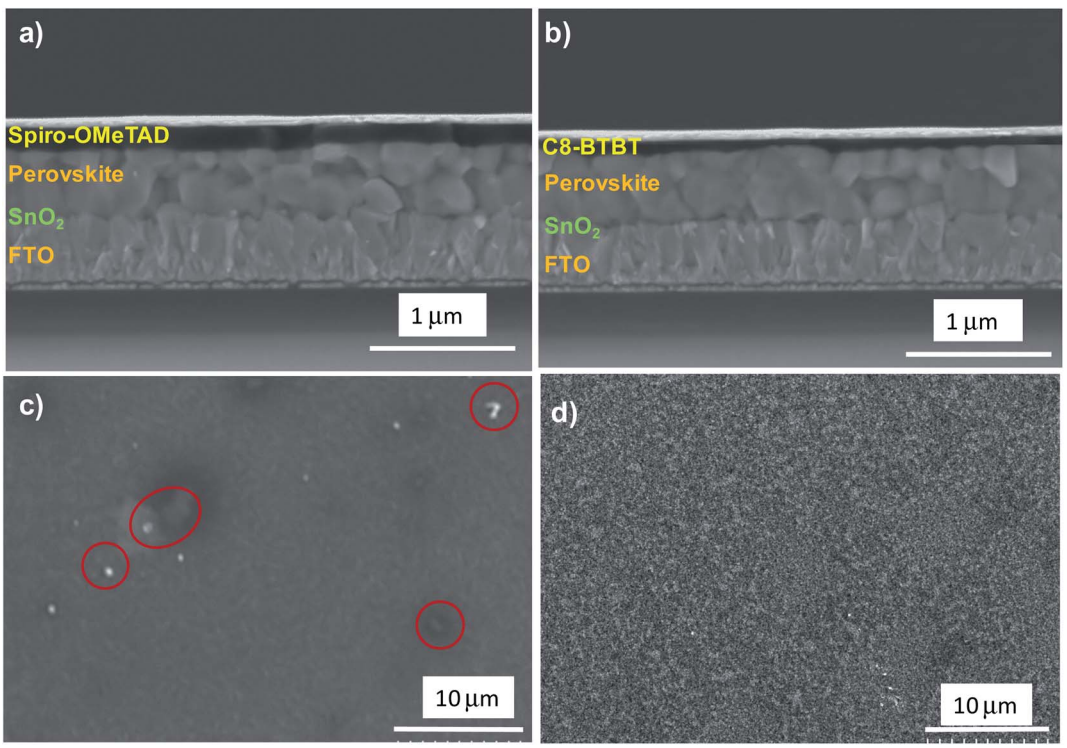

Fig. 2 Cross-sectional FE-SEM images of the completed device with (a) spiro-OMeTAD and (b) C8-BTBT HTLs. Top-view FE-SEM images of (c) spiro-OMeTAD and (d) C8-BTBT HTLs.

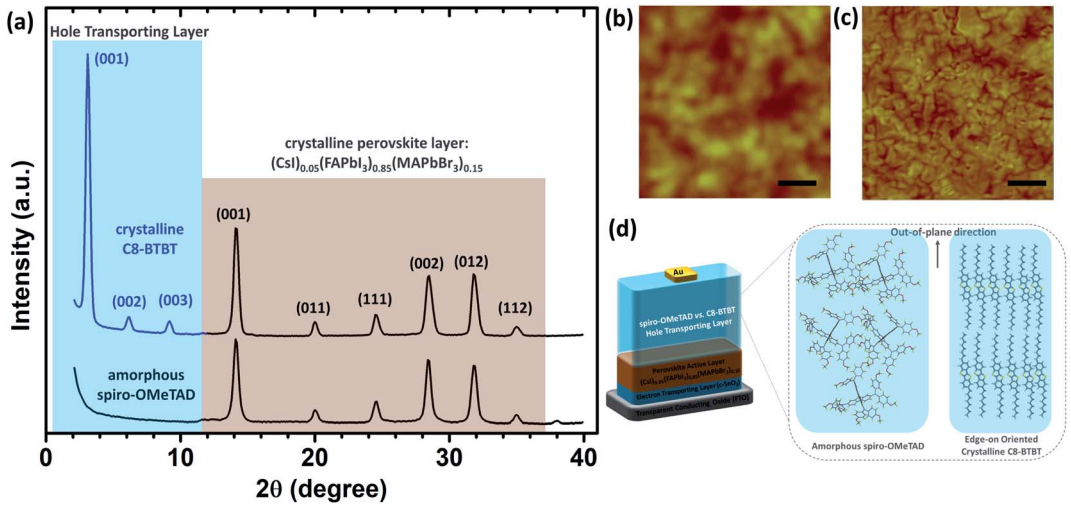

Fig. 3 (a) θ–2θ out-of-plane X-ray diffraction (XRD) scans and (b and c) tapping mode atomic force microscopy (AFM) topographic images for (FTO)/c-SnO_2/$(CsI)_{0.05}(FAPbI_3)_{0.85}(MAPbBr_3)_{0.15}$/spiro-OMeTAD (bottom XRD scan in (a) and (b)) and (FTO)/c-SnO_2/$(CsI)_{0.05}(FAPbI_3)_{0.85}(MAPbBr_3)_{0.15}$/C8-BTBT (top XRD scan in (a) and (c)) substrates. The crystalline planes in the out-of-plane direction for the C8-BTBT and spiro-OMeTAD hole transporting layers (HTL) (blue shaded area) and for the perovskite layer (brown shaded area) are shown in the XRD scans. The scale bars in the AFM images denote 1 μm. (d) A schematic of the edge-on oriented crystalline C8-BTBT HTL *vs.* the amorphous spiro-OMeTAD HTL in the out-of-plane direction with respect to the underlying perovskite layer. Note that the HTL film thickness in (d) is not to scale.

tapping mode atomic force microscopy (AFM) (Fig. 3(b) and (c)), which revealed that C8-BTBT forms a highly crystalline thin film with grain sizes of ~0.25–1 μm whereas the doped spiro-OMeTAD film consists of mainly amorphous granular domains (~0.1–0.4 μm in size). In both XRD scans, multiple diffraction peaks in the relatively high angle region ($2\theta \approx 10$–40°, the brown shaded area in Fig. 3(a)) corresponding to varied crystalline planes of the perovskite layer ((001), (011), (111), (002), (012), and (112)) were clearly evident. In the low angle region ($2\theta < 10^\circ$), while the spiro-OMeTAD HTL did not show any out-of-plane microstructural ordering (*i.e.*, amorphous), a strong diffraction peak at $2\theta = 3.10^\circ$ was observed for the C8-BTBT HTL along with its higher order peaks of (002) and (003). This indicates the presence of a highly crystalline long-range ordered C8-BTBT microstructure in the HTL. On the basis of the simulated powder XRD pattern (Fig. S4†) using the reported single-crystal structure of C8-BTBT,[37,52] an edge-on molecular orientation (BTBT π-backbone and octyl chains aligned in the out-of-plane direction) is proposed in the current HTL on the perovskite surface (Fig. 3(d)). This particular molecular orientation and densely packed morphology should be highly favorable for effective protection of the perovskite layer against ambient species *via* hydrophobicity (*vide infra*).

We first optimized the C8-BTBT spin-coating solution concentration. As shown in Fig. 4(a), the power conversion efficiency (PCE) of PSCs increased with increasing the solution concentration of C8-BTBT up to 15 mg mL^{-1}. This improvement can be explained by better molecular surface coverage on the perovskite film at higher concentrations, which prevents current leakage and provides a higher shunt resistance. However, the PCE was found to decrease again going to higher concentrations (15 → 20 mg mL^{-1}), which is attributed to the formation of a higher series resistance across the solar cell with increased thickness of the HTL.[53] As a result, the optimum hole transporting material (HTM) solution concentration was found to be 15 mg mL^{-1}, which was used for further device fabrications. As compared to the state-of-the-art spiro-OMeTAD HTM, which is typically used at a very high concentration of 90 mg mL^{-1}, such a low concentration for C8-BTBT exhibits an outstanding cost-effectiveness for device fabrication.

The current density–voltage (J–V) curves and photovoltaic parameters of the best performing PSCs fabricated with C8-BTBT and doped spiro-OMeTAD are shown in Fig. 4(b) and Table 1, respectively. The dopant-free C8-BTBT HTL-based solar cells achieved a PCE of up to 22.45% with an open-circuit voltage (V_{OC}) of 1145 mV, a short-circuit current (J_{SC}) of 24.21 mA cm^{-2}, and a fill factor (FF) of 82%. These values are relatively higher compared to the reference device fabricated with the same architecture with doped spiro-OMeTAD. The doped spiro-OMeTAD HTL-based PSCs exhibited a V_{OC} of 1094 mV, a J_{SC} of 24.02 mA cm^{-2}, and an FF of 75%, yielding a PCE of 19.84%. The better photovoltaic performance of the C8-BTBT based cell was associated with the increased V_{OC} and FF values but there was almost no change in the J_{SC}. The improvement in photovoltaic parameters of the cell cannot be explained by just one mechanism. Although it has been proven that the V_{OC} of PSCs is independent of the HOMO level of the HTMs,[54] it is known that the minimizing the energy barriers between the charge transporting and perovskite layers contributes to the V_{OC} and FF of the cells.[55,56] The lower HOMO level of C8-BTBT (−5.5 eV)[44] than that of spiro-OMeTAD (−5.0)[57] provides a better match with the valence band of the perovskite layer (~−5.5 eV).[58] Therefore, the low energy barriers between C8-BTBT and the perovskite layer contributes to efficient hole extraction. In addition, the high LUMO energy level of C8-BTBT (−2.0 eV) reduces charge carrier recombination at the interface.

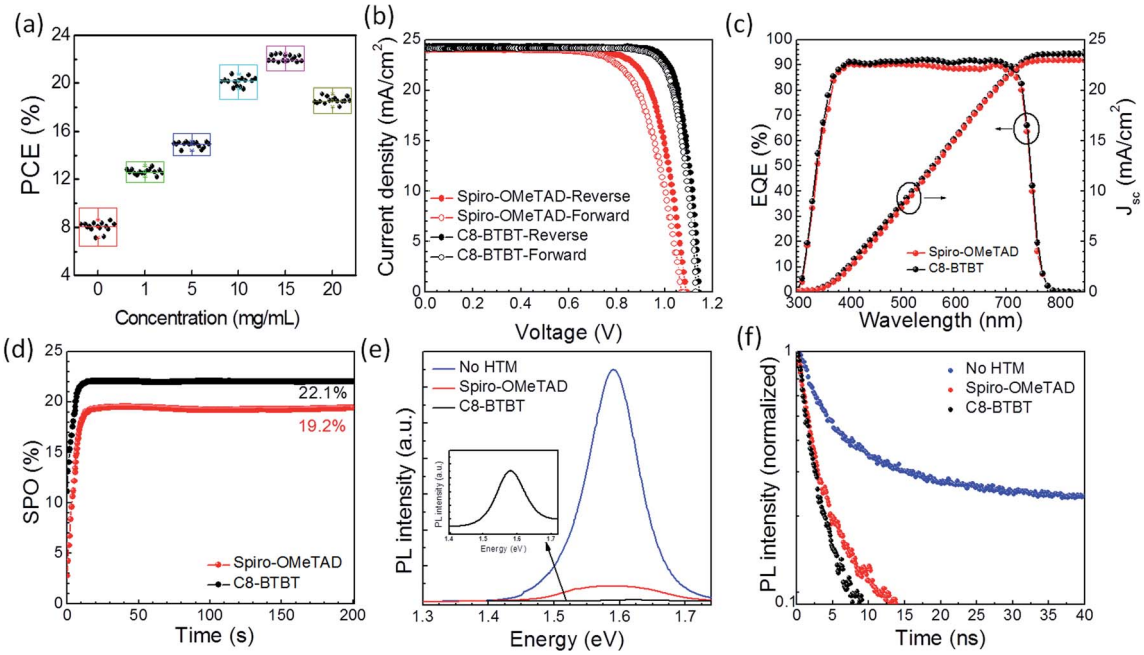

Fig. 4 (a) The obtained PCE values as a function of the C8-BTBT concentration. (b) *J–V* curves, (c) EQE curves and integrated J_{SC} values, and (d) MPP tracking for 200 s of the best performing devices fabricated with C8-BTBT and spiro-OMeTAD HTLs. (e) Steady-state and (f) time-resolved PL (TRPL) spectra of the perovskite films with and without HTLs.

The enhancement in the V_{OC} and FF of the cell can also be attributed to the defect passivation effect of the C8-BTBT molecules on the surface and the grain boundary of the perovskite layer due to the chemical interactions.[49] Moreover, higher hole mobility of C8-BTBT than that of spiro-OMeTAD is another factor that might lead to the enhancement of the FF.

It is worth noting that Zhao *et al.* recently employed C8-BTBT as an interfacial layer between the perovskite and spiro-OMeTAD films.[49] In that study, C8-BTBT clusters were irregularly accumulated on the perovskite surface, and some of the C8-BTBT on the surface was dissolved in spiro-OMeTAD solution during the spiro-OMeTAD coating step. Moreover, the utilization of spiro-OMeTAD as the HTL was still limiting the thermal stability of the devices. However, in our study, a 50 nm thick solution-processed C8-BTBT film was employed as the only HTL on the perovskite layer. The continuous and uniform C8-BTBT film formation on the surface of the perovskite layer provided better defect passivation on the surface and grain boundary of the perovskite layer. Moreover, the fabrication of PSCs without the spiro-OMeTAD layer reduced the device cost, simplified processing, and improved the stability of the cell (*vide infra*).

On the other hand, one of the key issues in PSCs is the mismatch of *J–V* curves between the forward (J_{SC} to V_{OC}) and reverse (V_{OC} to J_{SC}) scans, named as *J–V* hysteresis. As is clearly seen in Fig. 4(b) and Table 1, there were differences between the forward and reverse *J–V* scans for both solar cells. The hysteresis index (HI) of the cells was calculated according to the following equation:[59]

$$\mathrm{HI} = \frac{J_{RS}(0.8V_{OC}) - J_{FS}(0.8V_{OC})}{J_{RS}(0.8V_{OC})} \quad (1)$$

The HIs for the dopant-free C8-BTBT and doped spiro-OMeTAD HTL-based devices were calculated to be 0.018 and 0.027, respectively. This indicates a much smaller hysteresis for dopant-free C8-BTBT HTL-based devices, which could be explained with its better matched HOMO level and very high LUMO energy level that together prevents hole accumulation at the HTL-perovskite interface and undesired back electron transport from the perovskite active layer. Moreover, the dopant-free nature of the C8-BTBT HTL helps to improve the HI since dopants such as Li-TFSI are known to deteriorate hysteresis in PSCs due to ion migration (*e.g.*, Li^+).[60]

Table 1 Photovoltaic parameters of the best performing devices

HTL		J_{SC} (mA cm^{-2})	V_{OC} (mV)	FF	PCE (%)	HI
Spiro-OMeTAD	Reverse	24.02	1094	0.75	19.84	0.027
	Forward	23.99	1065	0.73	18.71	
C8-BTBT	Reverse	24.21	1145	0.82	22.45	0.018
	Forward	24.08	1130	0.80	21.76	

The external quantum efficiency (EQE) spectra and integrated current values for the best performing devices are shown in Fig. 4(c). Both devices displayed a prominent quantum yield in the 300–800 nm spectral region. The corresponding integrated J_{SC} values were determined to be 22.94 and 23.56 mA cm^{-2} for the cells fabricated with doped spiro-OMeTAD and dopant-free C8-BTBT HTLs, respectively. These values were in agreement with the J_{SC} values obtained from J–V measurements. Furthermore, by holding the cells under maximum power point tracking (MPPT) at a constant bias-voltage, we performed stabilized power output (SPO) measurements over time. As seen in Fig. 4(d), not only dopant-free C8-BTBT but also doped spiro-OMeTAD HTL-based devices showed stable outputs with PCEs of 22.1% and 19.2%, respectively, which are consistent with the values obtained from the J–V curves. In addition, the reproducibility of the PSCs was investigated by measuring the J–V of the devices, and the histogram charts of the cells with digital photographs are given in Fig. S5.† The efficiency distribution for the devices fabricated with dopant-free C8-BTBT was narrower than the doped spiro-OMeTAD HTL-based devices, indicating a better reproducibility for C8-BTBT. The difference probably originates from the fact that while dopant-free C8-BTBT HTL formation with the required electronic structure is quite reproducible since it does not require additional doping/oxidation, the formation of an electronic structure for the doped spiro-OMeTAD HTL relies on atmospheric oxidation that may show variations.

In order to gain more insights into the hole extraction properties of dopant-free C8-BTBT and doped spiro-OMeTAD HTLs, comparative steady-state photoluminescence (PL) and time-resolved photoluminescence (TRPL) measurements were carried out. As shown in Fig. 4(e), the intensity of the strong PL peak observed for bare perovskite was found to remarkably decrease (~10–15×) when coated with doped spiro-OMeTAD or dopant-free C8-BTBT films. Similarly, TRPL measurements showed much shorter PL decay lifetimes for HTL-coated perovskite active layers in Fig. 4(f). The average PL lifetime (t_{ave}) of pristine perovskite was about 82.12 ns which then decreased to 25.82 ns and 15.35 ns when the spiro-OMeTAD and C8-BTBT films was used as an HTL, respectively. These results revealed that both materials effectively extract the holes from the perovskite layer. Moreover, the shorter PL lifetime of perovskite/C8-BTBT than that of the perovskite/spiro-OMeTAD sample indicated that the C8-BTBT layer effectively reduced nonradiative recombination sites at the interface.[49]

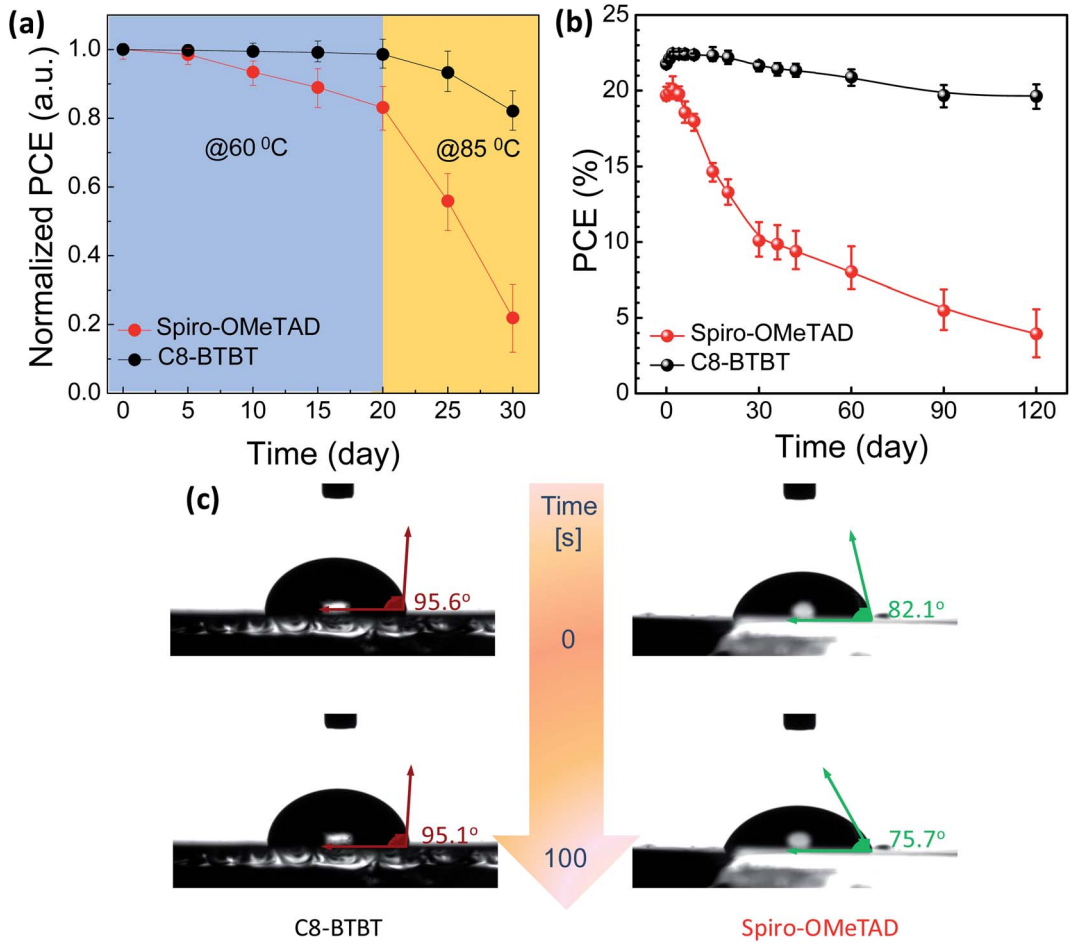

Fig. 5 (a) Thermal stability tests of the cells stressed at different temperatures. (b) The shelf life test in the ambient atmosphere for the unencapsulated devices fabricated with the spiro-OMeTAD and C8-BTBT HTLs (4 devices were monitored for each case). (c) The contact angle measurements of HTLs as a function of water loading time.

These results together revealed that photogenerated excitons in the perovskite layer could be effectively quenched by an adjacent HTL of doped spiro-OMeTAD or dopant-free C8-BTBT. Since there are no spectral overlaps between the perovskite's PL spectrum and HTL's absorption spectra, the quenching could not be through energy transfers but rather through very efficient perovskite-to-HTL interfacial hole extractions. It is noteworthy that, as expected from its higher PCE values in PSCs, dopant-free C8-BTBT coated perovskite showed slightly more efficient PL quenching and faster PL decays as compared to the doped spiro-OMeTAD HTL, which is ascribed to the reduction of interfacial energy barriers between the HTL and perovskite due to the matched HOMO level of C8-BTBT with the perovskite layer and the passivation effect of the C8-BTBT layer.

Finally, long-term thermal stabilities at two different temperatures (60 °C and 85 °C) and self-life stabilities of the un-encapsulated devices in an ambient environment (~40–45% RH) were investigated by periodically monitoring the *J–V* curve of the cells. As shown in Fig. 5(a), while the C8-BTBT based cell maintained its initial PCE at 60 °C for 20 days, the spiro-OMeTAD based cell lost 17% of its initial PCE which is probably due to the Au migration through to the spiro-OMeTAD at 60 °C.[61,62] In addition, the PCE of the spiro-OMeTAD based cell decreased drastically in 10 days when the temperature increased to 85 °C. It was not surprising when considering that the glass transition temperature (T_g) of spiro-OMeTAD decreases from ~154 °C to ~90 °C with the addition of Li-TFSI and TBP.[63] Therefore, crystallization of spiro-OMeTAD during the thermal aging experiment at 85 °C could decrease the hole mobility of spiro-OMeTAD.[64] On the other hand, the C8-BTBT-based cell lost only 18% of its initial PCE due to the more favorable thermal characteristics of C8-BTBT compared to doped spiro-OMeTAD.[41]

Moreover, while dopant-free C8-BTBT HTL-based devices maintained >80% of its initial efficiency after 120 days of storage at room temperature in ambient air (Fig. 5(b)), doped spiro-OMeTAD HTL-based solar cells were able to show only ~19% of its initial value. In order to understand the effect of hydrophobicity on the stability of PSCs, contact angle measurements as a function of water loading time were carried out. As shown in Fig. 5(c), the water contact angles for dopant-free C8-BTBT and doped spiro-OMeTAD films were measured to be 95.6° and 82.1°, respectively. While the water contact angle on the dopant-free C8-BTBT film remained almost the same after 100 s, that on doped spiro-OMeTAD films decreased to 75.7°. These results revealed the hydrophobic nature of the dopant-free C8-BTBT film. This is due to its densely packed microstructure with alkyl chains pointing towards the air-HTL interface, which acts as a physical barrier on the perovskite active layer against ambient species (especially moisture) penetration.[65]

Conclusions

In summary, C8-BTBT molecules that could be synthesized by a relatively straightforward three-step transition-metal-free process were applied for the first time as a dopant-free HTL in n–i–p PSCs. PSCs with PCEs of around 22.45% with negligible hysteresis were developed by using C8-BTBT molecules as the HTL. Furthermore, C8-BTBT improved ambient and thermal stability of the PSCs. While the reference cells with doped spiro-OMeTAD retained only 19%, 83%, and 22% of their initial PCE values at room temperature (120 days), at 60 °C (20 days), and at 85 °C (10 days), respectively, C8-BTBT-based PSCs maintained >80%, 99%, and 82% of their initial PCE values at room temperature (120 days), at 60 °C (20 days), and at 85 °C (10 days), respectively. Microstructural, morphological, and photophysical characterization studies revealed that dopant-free hydrophobic C8-BTBT thin film serves as a promising HTL to improve the ambient and thermal stability of PSCs. In a broader sense, our findings herein clearly demonstrate the outstanding potential of wide optical band gap BTBT-based semiconducting π-systems for highly stable dopant-free perovskite solar cell applications. Future molecular design efforts on the BTBT π-system, such as with side-chain engineering or polar/electron-donating/-withdrawing group functionalization, could further tune a dopant-free HTL microstructure and physicochemical/optoelectronic properties and may open up new avenues to simultaneously realize high efficiency and ambient stability. Particularly, a BTBT-based molecular semiconductor with a much lower density of σ-insulating alkyl chains and a polar functional group could facilitate face-on molecular growth at the perovskite–HTL interface for improved vertical charge extraction and transport characteristics.

Conflicts of interest

There are no conflicts to declare.

References

1 M. I. H. Ansari, A. Qurashi and M. K. Nazeeruddin, *J. Photochem. Photobiol., C*, 2018, **35**, 1–24.
2 R. Wang, M. Mujahid, Y. Duan, Z.-K. Wang, J. Xue and Y. Yang, *Adv. Funct. Mater.*, 2019, **29**, 1808843.
3 M. S. Jamal, M. S. Bashar, A. K. M. Hasan, Z. A. Almutairi, H. F. Alharbi, N. H. Alharthi, M. R. Karim, H. Misran, N. Amin, K. B. Sopian and M. Akhtaruzzaman, *Renewable Sustainable Energy Rev.*, 2018, **98**, 469–488.
4 S. Akin, E. Akman and S. Sonmezoglu, *Adv. Funct. Mater.*, 2020, **30**, 2002964.
5 C. C. Boyd, R. Cheacharoen, T. Leijtens and M. D. McGehee, *Chem. Rev.*, 2019, **119**, 3418–3451.
6 I. C. Kaya, K. P. S. Zanoni, F. Palazon, M. Sessolo, H. Akyildiz, S. Sonmezoglu and H. J. Bolink, *Adv. Energy Sustain. Res.*, 2021, **2**, 2000065.
7 B. Roose, Q. Wang and A. Abate, *Adv. Energy Mater.*, 2019, **9**, 1803140.
8 M. Salado, L. Contreras-Bernal, L. Caliò, A. Todinova, C. López-Santos, S. Ahmad, A. Borras, J. Idígoras and J. A. Anta, *J. Mater. Chem. A*, 2017, **5**, 10917–10927.
9 A. Culu, I. C. Kaya and S. Sonmezoglu, *ACS Appl. Energy Mater.*, 2022, **5**, 3454–3462.

10 S. Akin, Y. H. Liu, M. I. Dar, S. M. Zakeeruddin, M. Gratzel, S. Turan and S. Sonmezoglu, *J. Mater. Chem. A*, 2018, **6**, 20327–20337.
11 J. Li, Q. Dong, N. Li and L. Wang, *Adv. Energy Mater.*, 2017, **7**, 1602922.
12 S. Sonmezoglu and S. Akin, *Nano Energy*, 2020, **76**, 105127.
13 W. Zhang, L. Wan, X. Li, Y. Wu, S. Fu and J. Fang, *J. Mater. Chem. A*, 2019, **7**, 18898–18905.
14 S. Akin, F. Sadegh, S. Turan and S. Sonmezoglu, *ACS Appl. Mater. Interfaces*, 2019, **11**, 45142–45149.
15 H. D. Pham, T. C. J. Yang, S. M. Jain, G. J. Wilson and P. Sonar, *Adv. Energy Mater.*, 2020, **10**, 1903326.
16 K. Rakstys, C. Igci and M. K. Nazeeruddin, *Chem. Sci.*, 2019, **10**, 6748–6769.
17 B. Tu, Y. Wang, W. Chen, B. Liu, X. Feng, Y. Zhu, K. Yang, Z. Zhang, Y. Shi, X. Guo, H. F. Li, Z. Tang, A. B. Djurisic and Z. He, *ACS Appl. Mater. Interfaces*, 2019, **11**, 48556–48563.
18 R. Ozdemir, S. Park, İ. Deneme, Y. Park, Y. Zorlu, H. A. Alidagi, K. Harmandar, C. Kim and H. Usta, *Org. Chem. Front.*, 2018, **5**, 2912–2924.
19 I. Susic, K. P. S. Zanoni, A. Paliwal, I. C. Kaya, Z. Hawash, M. Sessolo, E. Moons and H. J. Bolink, *Sol. RRL*, 2022, 2100882.
20 Y. Li, M. D. Cole, Y. Gao, T. Emrick, Z. Xu, Y. Liu and T. P. Russell, *ACS Appl. Energy Mater.*, 2019, **2**, 1634–1641.
21 Q. Jiang, Y. Zhao, X. Zhang, X. Yang, Y. Chen, Z. Chu, Q. Ye, X. Li, Z. Yin and J. You, *Nat. Photonics*, 2019, **13**, 460–466.
22 Y. Wang, X. Liu, T. Zhang, X. Wang, M. Kan, J. Shi and Y. Zhao, *Angew. Chem., Int. Ed.*, 2019, **58**, 16691–16696.
23 S. Akin, Y. Altintas, E. Mutlugun and S. Sonmezoglu, *Nano Energy*, 2019, **60**, 557–566.
24 I. C. Kaya, S. Akin and S. Sonmezoglu, in *Sustainable Materials for Next Generation Energy Devices*, eds. K. Y. Cheong and L.-C. Chen, Elsevier, 2021, DOI: https://doi.org/DOI: **10.1016/B978-0-12-820628-7.00008-3**, pp. 181–219.
25 Z. Hawash, L. K. Ono and Y. Qi, *Adv. Mater. Interfaces*, 2016, **3**, 1600117.
26 Z. Li, C. Xiao, Y. Yang, S. P. Harvey, D. H. Kim, J. A. Christians, M. Yang, P. Schulz, S. U. Nanayakkara, C.-S. Jiang, J. M. Luther, J. J. Berry, M. C. Beard, M. M. Al-Jassim and K. Zhu, *Energy Environ. Sci.*, 2017, **10**, 1234–1242.
27 H. Xi, S. Tang, X. Ma, J. Chang, D. Chen, Z. Lin, P. Zhong, H. Wang and C. Zhang, *ACS Omega*, 2017, **2**, 326–336.
28 Q.-Q. Ge, J.-Y. Shao, J. Ding, L.-Y. Deng, W.-K. Zhou, Y.-X. Chen, J.-Y. Ma, L.-J. Wan, J. Yao, J.-S. Hu and Y.-W. Zhong, *Angew. Chem., Int. Ed.*, 2018, **57**, 10959–10965.
29 C. Shen, Y. Wu, H. Zhang, E. Li, W. Zhang, X. Xu, W. Wu, H. Tian and W.-H. Zhu, *Angew. Chem., Int. Ed.*, 2019, **58**, 3784–3789.
30 H. D. Pham, Z. Wu, L. K. Ono, S. Manzhos, K. Feron, N. Motta, Y. Qi and P. Sonar, *Adv. Electron. Mater.*, 2017, **3**, 1700139.
31 H. Zhu, Z. Shen, L. Pan, J. Han, F. T. Eickemeyer, Y. Ren, X. Li, S. Wang, H. Liu, X. Dong, S. M. Zakeeruddin, A. Hagfeldt, Y. Liu and M. Grätzel, *ACS Energy Lett.*, 2020, **6**, 208–215.
32 X. Sun, X. Deng, Z. Li, B. Xiong, C. Zhong, Z. Zhu, Z. Li and A. K. Jen, *Adv. Sci.*, 2020, **7**, 1903331.
33 Q. Fu, Z. Xu, X. Tang, T. Liu, X. Dong, X. Zhang, N. Zheng, Z. Xie and Y. Liu, *ACS Energy Lett.*, 2021, 1521–1532, DOI: **10.1021/acsenergylett.1c00385**.
34 R. Azmi, S. Y. Nam, S. Sinaga, Z. A. Akbar, C.-L. Lee, S. C. Yoon, I. H. Jung and S.-Y. Jang, *Nano Energy*, 2018, **44**, 191–198.
35 F. Zhang, X. Zhao, C. Yi, D. Bi, X. Bi, P. Wei, X. Liu, S. Wang, X. Li, S. M. Zakeeruddin and M. Grätzel, *Dyes Pigm.*, 2017, **136**, 273–277.
36 B. Tu, Y. Wang, W. Chen, B. Liu, X. Feng, Y. Zhu, K. Yang, Z. Zhang, Y. Shi, X. Guo, H.-F. Li, Z. Tang, A. B. Djurišić and Z. He, *ACS Appl. Mater. Interfaces*, 2019, **11**, 48556–48563.
37 H. Ebata, T. Izawa, E. Miyazaki, K. Takimiya, M. Ikeda, H. Kuwabara and T. Yui, *J. Am. Chem. Soc.*, 2007, **129**, 15732–15733.
38 T. Izawa, E. Miyazaki and K. Takimiya, *Adv. Mater.*, 2008, **20**, 3388–3392.
39 H. Usta, D. Kim, R. Ozdemir, Y. Zorlu, S. Kim, M. C. Ruiz Delgado, A. Harbuzaru, S. Kim, G. Demirel, J. Hong, Y.-G. Ha, K. Cho, A. Facchetti and M.-G. Kim, *Chem. Mater.*, 2019, **31**, 5254–5263.
40 X. Liu, I. Balla, V. K. Sangwan, H. Usta, A. Facchetti, T. J. Marks and M. C. Hersam, *Chem. Mater.*, 2019, **31**, 1761–1766.
41 T. Matsushima, A. S. D. Sandanayaka, Y. Esaki and C. Adachi, *Sci. Rep.*, 2015, **5**, 14547.
42 W. Wei, C. Yang, J. Mai, Y. Gong, L. Yan, K. Zhao, H. Ning, S. Wu, J. Gao, X. Gao, G. Zhou, X. Lu and J. M. Liu, *J. Mater. Chem. C*, 2017, **5**, 10652–10659.
43 W. Tu, T. Liu, Z. Zhang, G. Wu, H. Chen and M. Wang, *Synth. Met.*, 2016, **219**, 20–25.
44 X. Lian, J. Chen, Y. Zhang, G. Wu and H. Chen, *Chin. J. Chem.*, 2019, **37**, 1239–1244.
45 M. Yilmaz, M. Ozdemir, H. Erdogan, U. Tamer, U. Sen, A. Facchetti, H. Usta and G. Demirel, *Adv. Funct. Mater.*, 2015, **25**, 5669–5676.
46 S. Tong, J. Sun, C. Wang, Y. Huang, C. Zhang, J. Shen, H. Xie, D. Niu, S. Xiao, Y. Yuan, J. He, J. Yang and Y. Gao, *Adv. Electron. Mater.*, 2017, **3**, 1700058.
47 L. Li, S. Tong, Y. Zhao, C. Wang, S. Wang, L. Lyu, Y. Huang, H. Huang, J. Yang, D. Niu, X. Liu and Y. Gao, *ACS Appl. Mater. Interfaces*, 2018, **10**, 20959–20967.
48 H. Xia, S. Tong, C. Zhang, C. Wang, J. Sun, J. He, J. Zhang, Y. Gao and J. Yang, *Appl. Phys. Lett.*, 2018, **112**, 233301.
49 R. Zhao, L. Xie, R. Zhuang, T. Wu, R. Zhao, L. Wang, L. Sun and Y. Hua, *ACS Energy Lett.*, 2021, **6**, 4209–4219.
50 M. A. Khalily, H. Usta, M. Ozdemir, G. Bakan, F. B. Dikecoglu, C. Edwards-Gayle, J. A. Hutchinson, I. W. Hamley, A. Dana and M. O. Guler, *Nanoscale*, 2018, **10**, 9987–9995.
51 E. J. Juarez-Perez, M. R. Leyden, S. Wang, L. K. Ono, Z. Hawash and Y. Qi, *Chem. Mater.*, 2016, **28**, 5702–5709.

52 T. Izawa, E. Miyazaki and K. Takimiya, *Adv. Mater.*, 2008, **20**, 3388–3392.
53 G.-W. Kim, D. V. Shinde and T. Park, *RSC Adv.*, 2015, **5**, 99356–99360.
54 B. Dänekamp, N. Droseros, D. Tsokkou, V. Brehm, P. P. Boix, M. Sessolo, N. Banerji and H. J. Bolink, *J. Mater. Chem. C*, 2019, **7**, 523–527.
55 C. M. Wolff, P. Caprioglio, M. Stolterfoht and D. Neher, *Adv. Mater.*, 2019, **31**, 1902762.
56 M. Steponaitis, M.-G. La-Placa, İ. C. Kaya, G. Bubniene, V. Jankauskas, M. Daskeviciene, M. Sessolo, T. Malinauskas, H. J. Bolink and V. Getautis, *Sustainable Energy Fuels*, 2020, **4**, 5017–5023.
57 Z. Hawash, L. K. Ono and Y. Qi, *Adv. Mater. Interfaces*, 2018, **5**, 1700623.
58 M. Deepa, M. Salado, L. Calio, S. Kazim, S. M. Shivaprasad and S. Ahmad, *Phys. Chem. Chem. Phys.*, 2017, **19**, 4069–4077.
59 H.-S. Kim and N.-G. Park, *J. Phys. Chem. Lett.*, 2014, **5**, 2927–2934.
60 Z. Hawash, L. K. Ono and Y. Qi, *Adv. Mater. Interfaces*, 2018, **5**, 1700623.
61 K. Domanski, J.-P. Correa-Baena, N. Mine, M. K. Nazeeruddin, A. Abate, M. Saliba, W. Tress, A. Hagfeldt and M. Grätzel, *ACS Nano*, 2016, **10**, 6306–6314.
62 K. Domanski, E. A. Alharbi, A. Hagfeldt, M. Grätzel and W. Tress, *Nat. Energy*, 2018, **3**, 61–67.
63 J.-Y. Seo, H.-S. Kim, S. Akin, M. Stojanovic, E. Simon, M. Fleischer, A. Hagfeldt, S. M. Zakeeruddin and M. Grätzel, *Energy Environ. Sci.*, 2018, **11**, 2985–2992.
64 X. Zhao, H.-S. Kim, J.-Y. Seo and N.-G. Park, *ACS Appl. Mater. Interfaces*, 2017, **9**, 7148–7153.
65 G.-S. Ryu, Z. Chen, H. Usta, Y.-Y. Noh and A. Facchetti, *MRS Commun.*, 2016, **6**, 47–60.